

Optical Signatures and Quantum Geometry in Proximity-Induced Topological Superconductors

Myungjun Kang,^{1,2,3,*} Yogeshwar Prasad,^{1,*} Nikhil Danny Babu,^{1,*}

Rasoul Ghadimi,¹ Jae Hoon Kim,⁴ and Sangmo Cheon^{1,2,5,†}

¹*Department of Physics, Hanyang University, Seoul 04763, Korea*

²*High Pressure Research Center, Hanyang University, Seoul 04763, Korea*

³*Department of Physics, University of Wisconsin-Milwaukee, Milwaukee, Wisconsin 53201, USA*

⁴*Department of Physics, Yonsei University, Seoul 03722, Korea*

⁵*Research Institute for Natural Science, Hanyang University, Seoul 04763, Korea*

Proximity-induced superconductivity at topological insulator-superconductor (TI-SC) interfaces offers a promising route to topological superconductivity with Majorana boundary modes. However, probing the interfacial superconductivity at buried interfaces is challenging with conventional surface methods. Here, we present a theoretical study of the longitudinal optical response of a TI-SC heterostructure, focusing on the complex interface sheet conductance as a direct and layer-selective probe of the interfacial superconducting gap. Within a minimal TI-SC model, we demonstrate that proximity-induced superconductivity at the buried interface generates a two-dimensional topological superconducting phase supporting Majorana edge modes. Using a Bogoliubov-de Gennes slab model and the Kubo formalism, we compute the optical conductance and introduce a thickness-extrapolation protocol that isolates the interface contribution only. The resulting interface conductance exhibits a robust, thickness-independent coherence peak at an energy set by the proximity-induced gap, distinguishable from both the parent superconductor's pair-breaking feature and the ungapped Dirac cone on the top surface. We further demonstrate that the low-frequency spectral weight of this interface resonance obeys a quantum-metric sum rule, quantitatively linking the optical response to the quantum geometry of the proximized interfacial state. Our results propose terahertz/infrared spectroscopy of the interfacial sheet conductance as a non-invasive diagnostic of Majorana-hosting TI-SC interfaces.

INTRODUCTION

Superconductors (SCs) with nontrivial band topology—topological superconductors (TSCs)—support Majorana boundary excitations that obey non-Abelian statistics and are therefore promising building blocks for fault-tolerant quantum information processing [1–7]. It has been suggested that a TSC can be realized via a *p*-wave pairing gap [8], and therefore the most direct route to Majorana states is through an intrinsic *p*-wave SC. Although candidates such as $\text{Cu}_x\text{Bi}_2\text{Se}_3$ [9, 10] have been proposed, intrinsic *p*-wave superconductivity is known to be rare in nature and is typically fragile against disorder.

An alternative route is to engineer a TSC state at the interface between a three-dimensional topological insulator (TI) and a conventional *s*-wave Bardeen-Cooper-Schrieffer (BCS) SC via the proximity effect [11–16]. In such TI-SC heterostructures, superconducting correlations induced in the helical Dirac surface states can, in principle, drive an effective *p*-wave TSC that supports Majorana boundary modes. Such proximity-induced superconductivity has been reported in several classes of systems, including nanowire-based systems [17–19], Bi_2Se_3 thin films on NbSe_2 [20], $\text{Bi}_2\text{Se}_3/\text{Bi}_2\text{Te}_3$ heterostructures coupled to cuprates [21]. Moreover, angle-resolved photoemission spectroscopy on a $\text{Pb}(111)/\text{TiBiSe}_2$ heterostructure showed that the Dirac surface state of the TI substrate migrates into the Pb overlayer and becomes gapped below the Pb's superconducting transition temperature [15]. In addition, Josephson transport, unconventional current-phase relations, anomalous Fraunhofer patterns, and scanning tunneling measurements reporting vortex-

core zero-bias states have all been interpreted as signatures of proximity-induced TSC in TI-based platforms [22–24], although a widely accepted and unambiguous identification of Majorana boundary modes remains elusive.

Optical and terahertz spectroscopy provide a noninvasive, contactless, and interface-sensitive probe that, in principle, can disentangle surface, interface, and bulk contributions to the electromagnetic response and access the energy scales associated with proximity-induced gaps. In standalone three-dimensional TIs, terahertz and optical measurements on Bi-based compounds have revealed surface-dominated low-frequency transport and complex in-plane optical conductivities arising from the interplay between bulk carriers and topological surface states [25–27]. By contrast, the frequency-dependent optical response and interface electrodynamics of TI-SC heterostructures remain comparatively unexplored. In thin-film geometries, the relevant observables are naturally expressed in terms of a complex sheet conductance $G(\omega)$, obtained by integrating the depth-dependent bulk conductivity $\sigma(\omega, z)$ over the sample thickness, providing a direct route to isolate the contribution of proximity-induced interface superconductivity and to search for decisive terahertz or infrared signatures of interfacial TSC states.

Beyond the search for spectroscopic fingerprints of interface superconductivity, a complementary perspective emerges from the viewpoint of band quantum geometry. In addition to the topological concepts such as the Berry curvature, the quantum metric—which quantifies distances between Bloch eigenstates on the quantum-state manifold—has become a key ingredient governing the response of multiband SCs and flat-band systems [28–30]. In such systems, the interband contribution to the superfluid weight is controlled by the Brillouin-

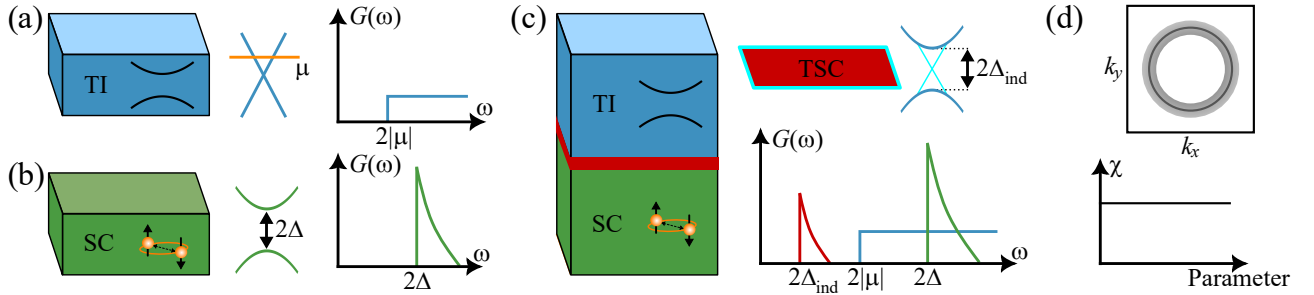


FIG. 1. Schematics of the TI-SC heterostructure and its optical and quantum-geometric signatures. (a) Isolated topological insulator (TI) with a gapped bulk and a gapless Dirac surface state. The chemical potential μ (orange) intersects the Dirac cone, producing a Pauli-blocked, step-like in-plane optical conductance $G_{xx}(\omega)$ with onset at $2|\mu|$. (b) Isolated conventional s -wave BCS superconductor (SC) with pairing amplitude Δ . Its optical response is gapped below 2Δ and exhibits a coherence peak at the gap edge. (c) TI-SC heterostructure obtained by placing the TI (blue) on top of the SC (green). The interface region (red) becomes a two-dimensional TSC that supports Majorana edge modes (cyan). Proximity pairing opens an induced gap $2\Delta_{\text{ind}}$ in the TI surface Dirac cone. The resulting heterointerface conductance $G_{xx}(\omega)$ shows a coherence peak at $2\Delta_{\text{ind}}$, a second peak at 2Δ from the bulk SC, and a Pauli-blocking contribution from the ungapped top-surface Dirac cone. (d) Quantum-geometric characterization and optical-conductance sum rule. The gray ring in momentum space marks the region where the quantum metric $g_{xx}(\mathbf{k})$ of the proximitized Dirac surface state is strongly enhanced due to the proximity-induced gap. The associated quantum weight $K_{\mu\mu} \propto \int_{\text{BZ}} d^2\mathbf{k} g_{\mu\mu}(\mathbf{k})$ is connected to the generalized optical weight through the sum rule $\int_0^\infty d\omega \text{Re}[G_{\mu\mu}(\omega)]/\omega \propto K_{\mu\mu}$. As a result, the dimensionless ratio χ between these two quantities remains essentially unchanged under variations of key parameters, such as the chemical potential and the proximity-coupling strength.

zone integral of the quantum metric and can even dominate the phase stiffness, thereby constraining attainable critical temperatures and the robustness of supercurrent. When a two-dimensional TSC state forms at a TI-SC heterointerface, the proximity-induced pairing gap that opens on the Dirac surface state fundamentally reshapes the quantum geometry of the Bogoliubov-de Gennes (BdG) bands [11]. The induced gap generates a distinct low-frequency optical response associated with interband transitions across the gapped Dirac cone and simultaneously creates a quantum-metric hotspot in momentum space, reflecting a strong redistribution of electronic character between electron-like and hole-like sectors near the interface gap [31–33]. Recent theoretical work has established a quantitative correspondence between this quantum metric—integrated over the Brillouin zone to yield the so-called quantum weight—and infrared optical spectral weight through sum rules that relate the metric to frequency integrals of the optical conductivity/conductance [32]. These developments highlight terahertz and infrared spectroscopy as direct, experimentally accessible probes of quantum geometry in superconducting heterostructures [28], and suggest that the optical response of TI-SC interfaces encodes both the presence of proximity-induced gaps and the underlying quantum geometry of the interfacial TSC state.

Here, we present a theoretical study of the longitudinal optical response of a TI-SC heterostructure, focusing on the complex heterointerface conductance $G_{xx}(\omega)$ as a direct probe of proximity-induced superconductivity. Within a minimal model that couples the Dirac surface state of a TI to a conventional s -wave BCS SC, we show that the proximitized interface realizes a two-dimensional TSC phase supporting Majorana edge modes.

We consider a system constructed of a simple TI model

with surface Dirac cones that result in Pauli blocking in the optical response [Fig. 1(a)], and a BCS SC that shows a coherence peak at the superconducting gap 2Δ in its optical response [Fig. 1(b)]. The TI is placed on top of the SC, resulting in the TI-SC heterostructure given in Fig. 1(c). The red heterointerface realizes a two-dimensional time-reversal invariant TSC hosting helical Majorana edge modes (cyan) in the effective model, while the induced gap of the heterointerface, $2\Delta_{\text{ind}}$, gaps out the Dirac cone that was present as the TI surface state. We show that the conductance spectrum exhibits two coherence peaks at $2\Delta_{\text{ind}}$ and 2Δ as well as a Pauli blocking response due to the Dirac cone state on the top surface, the schematics of which can be seen in Fig. 1(c). Using a microscopic slab model that resolves both surface and bulk electronic states, we evaluate the frequency-dependent sheet conductance $G_{xx}(\omega)$ and separate contributions from the surface and bulk optical channels. The calculations reveal a pronounced, thickness-independent resonance in the optical spectrum arising from the induced gap on the Dirac surface states, which directly reflects the surface-localized nature of the proximity pairing. Our approach provides a controlled protocol to disentangle interfacial and bulk responses, yielding a clear optical signature of proximity-induced interface superconductivity.

We also demonstrate via a sum rule of the optical conductance [32, 34] that the majority of the contribution to the quantum weight of the heterointerface bands appears due to the induced gap. The emergence of the TSC in the heterointerface results in an accumulation of large quantum metric near the superconducting gap. Based on the sum rule, we also show that the quantum weight of the system and the low-frequency integral $\int d\omega \text{Re}[G_{xx}(\omega)]/\omega$ preserve the same ratio regardless of the change in the various parameters of the system such

as the chemical potential and proximity interaction strength, the schematics of which can be seen in Fig. 1(d).

Our results demonstrate that terahertz and infrared spectroscopy provide a noninvasive, layer-selective means to detect proximity-induced topological superconductivity and to access the geometric properties of Majorana-hosting TI-SC heterostructures. This approach offers a practical pathway to observing optical fingerprints of Majorana physics and to quantitatively linking interfacial superconductivity with its underlying quantum geometry.

RESULTS

Proximity-Induced TSC at a TI-SC Heterointerface

We model the TI-SC heterostructure using a minimal lattice Hamiltonian in which a three-dimensional TI is coupled to a conventional *s*-wave SC. As both subsystems respect time-reversal symmetry, the TI realizes a nontrivial \mathbb{Z}_2 phase with a single helical Dirac surface state, while the SC provides a fully gapped order parameter. Coupling these subsystems via a common interface induces proximity-induced pairing among the Dirac fermions. In a slab geometry, we stack a TI layer of thickness l_T on top of an SC layer of thickness l_S along the z direction, producing a single buried interface where the Dirac surface state hybridizes with the superconducting layer [Fig. 1(c)]. This proximitized interface defines an effective two-dimensional superconducting region, whose topology we characterize below and whose longitudinal sheet conductance $G_{xx}(\omega)$ we analyze.

The normal-state electronic structure of the three-dimensional TI is described by the tight-binding (TB) Hamiltonian

$$H_{\text{TI}}(\mathbf{k}) = \left(m_0 + t_0 \sum_{i=x,y,z} \cos k_i \right) \tau_z + \alpha \sum_{i=x,y,z} \sin k_i \tau_x \sigma_i, \quad (1)$$

where τ_i and σ_j are Pauli matrices acting in orbital and spin space, respectively. The parameters m_0 and t_0 denote the on-site mass and nearest-neighbor hopping amplitudes, while α controls the strength of the spin-orbit coupling (SOC). Inversion and time-reversal symmetries are implemented as $P = \tau_z$ and $T = -i\sigma_y K$, respectively, where K denotes complex conjugation.

Because the TI is centrosymmetric and time-reversal invariant, its bulk band topology is encoded in a \mathbb{Z}_2 index ν that can be determined from the parity eigenvalues of the occupied bands at the time-reversal-invariant momenta (TRIM) Γ_i [35]. This index is given by

$$(-1)^\nu = \prod_{i \in \text{TRIM}} \prod_{m=1}^{N_{\text{occ}}} \xi_{2m}(\Gamma_i), \quad (2)$$

where $\xi_{2m}(\Gamma_i) = \pm 1$ is the parity eigenvalue of the $2m$ th occupied Kramers' pair at TRIM Γ_i , and N_{occ} denotes the num-

ber of occupied Kramers' pairs. The individual products at each TRIM are summarized in Fig. 2(a). A single band inversion occurs at the Γ point, indicating that the bulk is in a TI phase. For a slab geometry that is finite along z but periodic in x and y , the corresponding surface Brillouin zone is a square with surface TRIM \bar{K} , and the band inversion at Γ yields a single Dirac cone centered at $\bar{\Gamma}$, as highlighted by the blue surface band in Fig. 2(b).

The SC is modeled as a spin-degenerate single-band *s*-wave BCS SC with onsite pairing, described by the BdG Hamiltonian

$$H_{\text{SC}} = \left[-\mu + \sum_i (m + t \cos k_i) \right] \xi_z + \Delta \xi_y \sigma_y. \quad (3)$$

Here, ξ_i denote Pauli matrices in Nambu (particle-hole) space and σ_i act on the spin degree of freedom. The parameter μ is the chemical potential, m and t set the lattice-regularized normal-state dispersion, and Δ is the uniform onsite *s*-wave pairing amplitude. Expanding the cosine dispersion near the Γ point yields an approximately parabolic spin-degenerate band centered at Γ , and the resulting superconducting state is fully gapped and topologically trivial in the absence of coupling to the TI [Fig. 2(c)]. Time-reversal symmetry acts as $T = -i\sigma_y K$, and inversion is represented by $P = \tau_z$ in the orbital subspace, where τ_i are Pauli matrices in orbital space.

We now bring the TI and SC into contact along the z direction to form a TI-SC heterostructure, with the TI stacked on top of the SC [Fig. 1(c)]. In this geometry, the Dirac surface state localized at the bottom surface of the TI hybridizes with the top surface of the SC, while translation symmetry is preserved in the in-plane directions.

The total BdG Hamiltonian for the heterointerface takes the block form

$$H_{\text{HI}}(\mathbf{k}) = \begin{pmatrix} H_{\text{SC}}^S(\mathbf{k}) & H_I \\ H_I^\dagger & H_{\text{TI}}^S(\mathbf{k}) \end{pmatrix}, \quad (4)$$

where H_{TI}^S denotes the low-energy Dirac BdG theory of the TI surface, while H_{SC}^S is a minimal two-dimensional BdG model representing the SC surface states relevant for hybridization. H_I encodes the local hybridization across the interface. For simplicity, we assume that only the two surfaces forming the heterointerface are coupled, so that bulk states away from the interface remain unaffected.

The low-energy surface Dirac cone on the TI side is described by the effective BdG Hamiltonian

$$H_{\text{TI}}^S(\mathbf{k}) = -\mu \xi_z - \alpha k_x \sigma_y - \alpha k_y \xi_z \sigma_x, \quad (5)$$

where ξ_i acts in Nambu space and σ_j in spin space [see Sec. S1.1 for details]. This Hamiltonian captures a single Dirac cone with spin-momentum locking in the plane of the interface. We model the SC surface as a simple two-dimensional Hamiltonian and take the interface coupling to be a local hybridization $H_I = \lambda \xi_z$, which mixes electron and hole sectors across the interface. Integrating out the SC degrees of freedom using a Schrieffer-Wolff transformation [36],

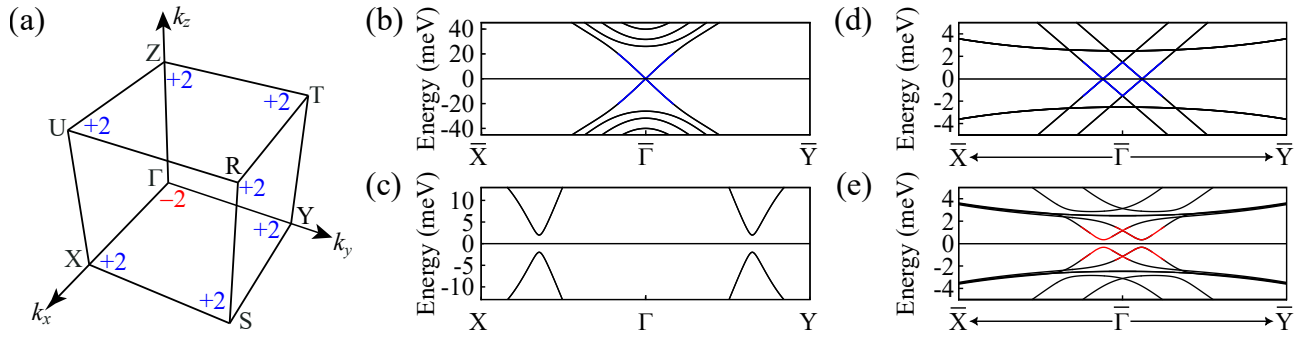


FIG. 2. Topological characteristics and band structures of the TI-SC heterostructure. (a) Parity eigenvalues of the occupied bands at the time-reversal-invariant momenta (TRIM) for the tight-binding TI model. A single band inversion at Γ identifies the bulk as a TI. (b) Surface band structure of a TI slab finite along z and periodic in the in-plane directions. The resulting Dirac surface state at $\bar{\Gamma}$ is highlighted in blue. (c) Bulk band structure of the s -wave SC, which is fully gapped and topologically trivial. (d) Band structure of the TI-SC heterostructure near the $\bar{\Gamma}$ point for vanishing interface hybridization $\lambda = 0$. The TI Dirac surface state (blue) remains gapless and decoupled from the SC bands. (e) Band structure of the heterostructure for finite interface coupling $\lambda = 3$. Hybridization with the SC induces superconducting pairing in the TI surface Dirac cone, opening a proximity-induced gap (red) and producing a fully gapped interface spectrum consistent with the effective BdG surface theory in Eq. (6). Representative parameters are $m_0 = -120$ meV, $t_0 = 48$ meV, $\alpha = 40$ meV, $m = -45$ meV, $t = 30$ meV, $\Delta = 2$ meV, $\mu = 1.5$ meV, with slab thicknesses $l_T = 8$ for the TI and $l_S = 8$ for the SC.

we obtain the low-energy effective Hamiltonian for the TI-SC heterointerface,

$$\bar{H}_{\text{TI}}^S(\mathbf{k}) = -\mu\xi_z - \alpha k_x \xi_z \sigma_y - \alpha k_y \sigma_x + \Delta_s \xi_y \sigma_y + \Delta_p (k_x \xi_y + k_y \xi_x \sigma_z), \quad (6)$$

where Δ_s and Δ_p represent proximity-induced s -wave and effective p -wave pairings on the TI surface, respectively. These quantities can be expressed analytically in terms of the microscopic parameters of the TI, SC, and interface coupling λ [see Sec. S1.2 for details].

The effect of the proximity coupling is illustrated in Figs. 2(d,e). In the absence of interface hybridization ($\lambda = 0$), the TI-SC heterostructure band structure simply consists of the ungapped Dirac surface state (blue) and the decoupled SC bands [Fig. 2(d)]. Upon turning on a finite interface coupling, $\lambda = 3$ meV, the Dirac cone at the heterointerface acquires a superconducting gap (red) due to the induced pairing, which we denote by Δ_{ind} [Fig. 2(e)]. For representative parameters $m_0 = -120$ meV, $t_0 = 48$ meV, $\alpha = 40$ meV, $m = -45$ meV, $t = 30$ meV, $\Delta = 2$ meV, and $\mu = 1.5$ meV, with TI thicknesses $l_T = 8$ and $l_S = 8$, the interface spectrum is fully gapped and adiabatically connected to the low-energy effective model in Eq. (6). For this choice of parameters, the induced gap extracted from Fig. 2(e) is $\Delta_{\text{ind}} \approx 0.355$ meV, significantly smaller than the parent pairing amplitude Δ , as expected for a proximity-induced gap. Note that although λ seems large, the resulting induced gap indicates that it acts as a perturbative parameter [see Eq. (S13)].

The momentum-dependent p -wave component Δ_p in Eq. (6) endows the proximitized surface with nontrivial topological order. To make this explicit, we derive the effective edge theory of the heterointerface and obtain analytic expressions for the Majorana edge modes. For an interface that is finite along x and y with open boundaries, we distinguish edges

by their outward normal. We label $i = 1$ ($i = 2$) as the edges normal to y (x), so that the corresponding low-energy modes propagate along x (y); in this notation, the edge Hamiltonian takes the form

$$H_i^{\text{edge}}(k_i) = (-1)^i k_i (\alpha \xi_y + \Delta_p \xi_x), \quad (7)$$

where ξ_i is the effective Nambu space, and the dispersion is

$$\varepsilon(k_i) = \pm k_i \sqrt{\alpha^2 + \Delta_p^2}. \quad (8)$$

In the projected low-energy subspace of a single helical Dirac channel, the edge theory reduces to an effective two-component Nambu spinor. The resulting edge eigenstates satisfy the Majorana constraint $\psi = \mathcal{C}\psi$ with $\mathcal{C} = \xi_x K$ (up to a basis convention). The corresponding edge-localized eigenstates can be written as

$$\psi_1^{\text{edge}} = \begin{pmatrix} e^{i\theta} \\ e^{-i\theta} \end{pmatrix}, \quad \psi_2^{\text{edge}} = \begin{pmatrix} e^{i\phi} \\ e^{-i\phi} \end{pmatrix}, \quad (9)$$

where the phases are defined by

$$\theta = \tan^{-1} \frac{\Delta_p - \sqrt{\Delta_p^2 + \alpha^2}}{\Delta_p}, \quad \phi = \frac{\pi}{2} + \theta. \quad (10)$$

These edge states satisfy a Majorana condition under particle-hole conjugation, confirming that the heterointerface realizes an effective time-reversal-invariant TSC with helical Majorana edge modes [see Sec. S1.2 for a full derivation].

Optical Response of the TI-SC Heterostructure

We first characterize the longitudinal optical response of an isolated TI slab, which serves as a baseline for analyzing

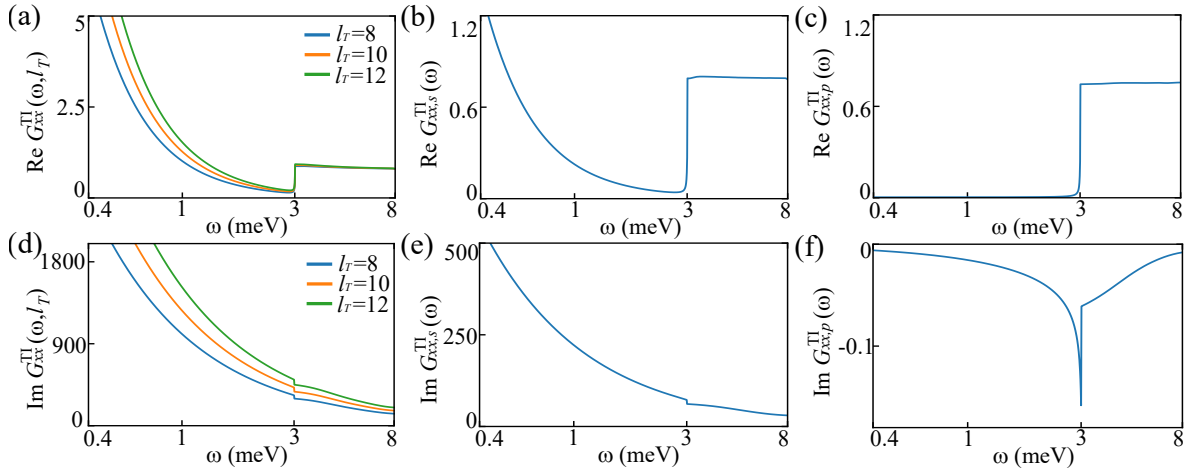


FIG. 3. **Optical response of a topological-insulator slab and extraction of the surface sheet conductance.** (a,d) Real and imaginary parts of the longitudinal conductance $G_{xx}^{\text{TI}}(\omega, l_T)$ (normalized by $G_0 = e^2/h$) for several TI slab thicknesses l_T . The spectra show a thickness-dependent Drude contribution and interband background, together with a Pauli-blocked onset at $\omega = 2|\mu|$ associated with the Dirac surface state. (b,e) Thickness-independent sheet conductance $G_{xx,s}^{\text{TI}}(\omega)/G_0$ obtained by extrapolating $G_{xx}^{\text{TI}}(\omega, l_T)/G_0$ to zero thickness. (c,f) Interband surface sheet conductance $G_{xx,p}^{\text{TI}}(\omega)/G_0$ obtained from the projected single-particle eigenstates onto the outermost TI layers (top and bottom surfaces), thereby isolating a surface-only optical channel. The close correspondence between panels (b) and (c) confirms that the Dirac surface response can be regarded as a two-dimensional conducting sheet superimposed on a bulk background that scales with l_T . Model parameters are the same as in Fig. 2.

the proximity-coupled heterostructure. The slab is taken to be open along the z direction and periodic in the (x, y) plane, and the complex longitudinal sheet conductance $G_{xx}^{\text{TI}}(\omega, l_T)$ is evaluated within linear response using the Kubo formalism in the single-particle eigenbasis. Throughout, we report conductivities and sheet conductances in units of $G_0 = e^2/h$ [see Methods for details of the numerical implementation].

For a given TI thickness l_T , the real part $\text{Re } G_{xx}^{\text{TI}}(\omega, l_T)$ exhibits a low-frequency Drude response together with a broad interband background originating from bulk and surface bands [Fig. 3]. Both contributions grow approximately linearly with l_T , reflecting the increasing number of TI bulk states participating in optical response. Superimposed on this bulk-like response, the Dirac surface cone generates a characteristic step-like structure. For $\omega < 2|\mu|$, interband transitions are Pauli blocked and the conductance remains strongly suppressed, whereas for $\omega > 2|\mu|$ these transitions are allowed and the spectrum rises into a broad plateau [Figs. 3(a,b)]. The imaginary part $\text{Im } G_{xx}^{\text{TI}}(\omega, l_T)$ shows the corresponding low-frequency $1/\omega$ -like behavior associated with the Drude term, as well as a dispersive kink near $\omega \simeq 2|\mu|$ set by the Dirac interband threshold [Figs. 3(d,e)].

To isolate the surface contribution, we treat the TI thickness l_T as a control parameter and fit the thickness dependence of $G_{xx}(\omega, l_T)$ to the linear form

$$G_{xx}^{\text{TI}}(\omega, l_T) = G_{xx,s}^{\text{TI}}(\omega) + \sigma_{xx}^{\text{TI}}(\omega) l_T, \quad (11)$$

where $G_{xx}^{\text{TI}}(\omega, l_T)$ is thickness-dependent conductance, $G_{xx,s}^{\text{TI}}(\omega)$ is thickness-independent sheet conductance, and $\sigma_{xx}^{\text{TI}}(\omega)$ is the bulk conductivity. This procedure cleanly separates the bulk contribution $\sigma_{xx}^{\text{TI}}(\omega)$ from the thickness-

independent sheet conductance $G_{xx,s}^{\text{TI}}(\omega)$, as illustrated in Figs. 3(b,e). In practice, we allow a quadratic term in the thickness fit, as detailed in Methods and Sec. S3. Table S1 shows that the quadratic term is negligible in the frequency window of interest, and we therefore use the linear form in the main text for clarity.

As an independent validation of this thickness-scaling procedure, we additionally construct a surface-only optical channel by projecting the slab eigenstates onto the outermost TI layers (top and bottom surfaces) when evaluating the Kubo kernel. This layer projection yields an interband surface sheet conductance, $G_{xx,p}^{\text{TI}}(\omega)$, that directly captures the Dirac-surface absorption with its Pauli-blocked threshold at $\omega = 2|\mu|$ [Figs. 3(c,f)]. The close agreement between the projected surface spectrum and the thickness-extrapolated sheet response demonstrates that the Dirac surface contribution behaves as a genuine two-dimensional conducting sheet superimposed on a bulk background that scales with l_T .

We next analyze the optical response of an isolated superconducting slab, which is shown in Fig. S2 of Sec. S2. In this case, the characteristic energy scale is set by the Bogoliubov-de Gennes gap Δ of the parent s -wave SC. In the clean-limit BCS picture, the real part $\text{Re } G_{xx}^{\text{SC}}(\omega)$ exhibits an optical gap for $0 < \omega \lesssim 2\Delta$, with vanishing regular absorption below 2Δ and a pronounced coherence peak at $\omega \simeq 2\Delta$ where pair-breaking excitations first become allowed. For $\omega > 2\Delta$, the conductance evolves into a gapped quasiparticle continuum. The imaginary part $\text{Im } G_{xx}^{\text{SC}}(\omega)$ displays the familiar superconducting behavior. A strong $1/\omega$ divergence at low frequencies associated with the superfluid stiffness, together with a dispersive feature near $\omega \simeq 2\Delta$, linked to the coherence peak.

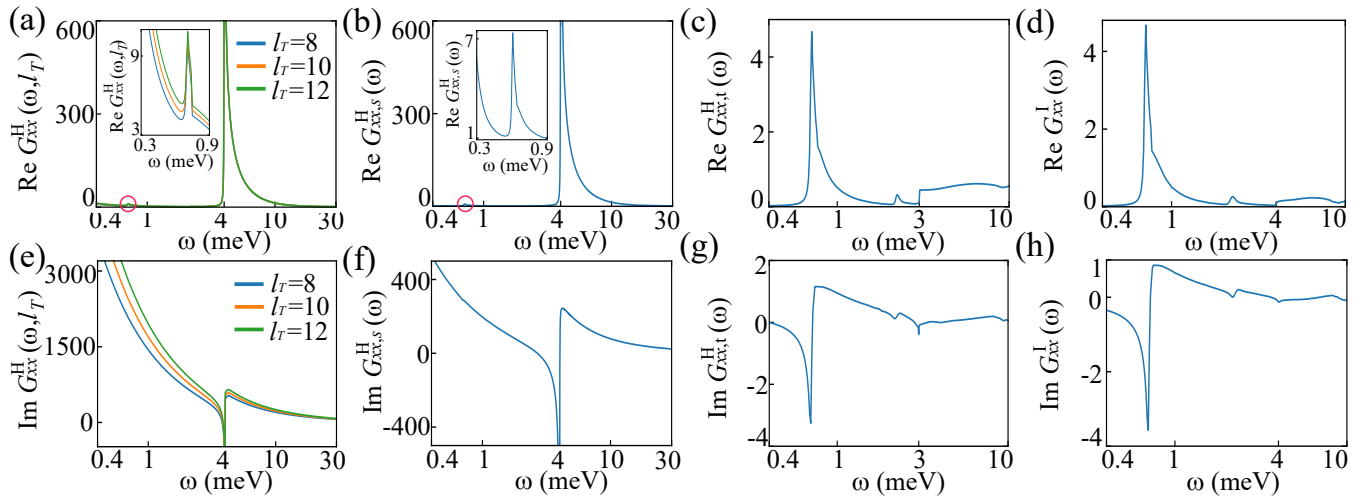


FIG. 4. **Optical response of the TI-SC heterostructure and isolation of the interface sheet conductance.** (a,e) Real and imaginary parts of the total in-plane sheet conductance $G_{xx}^H(\omega, l_T)/G_0$ of the TI-SC heterostructure for several TI thicknesses l_T . The spectra contain the TI bulk Drude response and Dirac surface contribution together with the proximitized interface states (highlighted in the insets, red circles). (b,f) Thickness-independent sheet component $G_{xx,s}^H(\omega)/G_0$ obtained by extrapolating $G_{xx}^H(\omega, l_T)/G_0$ as l_T goes to zero, thereby removing the TI bulk background that scales with thickness and retaining the combined sheet response of the top TI surface, the buried interface, and the SC slab. (c,g) Normalized surface sheet conductance $G_{xx,t}^H(\omega)/G_0$ after subtracting the calibrated SC sheet and bulk contributions, so that the remaining response arises from the top TI surface and the buried interface. (d,h) Interface-only sheet conductance $G_{xx}^I(\omega)/G_0$ obtained by further subtracting the known TI top-surface spectrum from the surface term in (c,g). This response consists of a single, sharply defined resonance at $\omega \simeq 2\Delta_{\text{ind}}$, identifying the induced coherence peak as an intrinsic property of the proximitized Dirac interface states rather than of TI or SC bulk channels. Model parameters are the same as in Fig. 2.

Both the superfluid weight and the quasiparticle continuum increase with the superconducting slab thickness l_S , confirming their bulk origin [Figs. S2(a,d)]. To disentangle surface and bulk contributions, we apply the thickness-extrapolation protocol in Sec. S3 and fit the superconducting sheet conductance to the form

$$G_{xx}^{\text{SC}}(\omega, l_S) = G_{xx,s}^{\text{SC}}(\omega) + \sigma_{xx}^{\text{SC}}(\omega) l_S, \quad (12)$$

which yields a thickness-independent sheet term $G_{xx,s}^{\text{SC}}(\omega)$ [Figs. S2(b,e)] and a bulk conductivity $\sigma_{xx}^{\text{SC}}(\omega)$ from the linear slope [Figs. S2(c,f)]. These calibrated superconducting responses serve as reference baselines for interpreting the optical conductance of the TI-SC heterostructure.

Having established the standalone TI and SC responses, we now turn to the full TI-SC heterostructure, in which the TI slab is stacked on top of a conventional SC [Fig. 4]. The total in-plane sheet conductance $G_{xx}(\omega, l_T)$ again displays a low-frequency Drude contribution together with a broad bulk-like background, both of which increase with the TI thickness l_T , as expected from the growing TI volume [Figs. 4(a,e)]. Superimposed on these contributions, a new low-frequency resonance emerges near the induced gap $2\Delta_{\text{ind}}$ of the proximitized interface states, as highlighted in the inset of Fig. 4(a).

To isolate the buried-interface response, we exploit the thickness dependence of the optical conductance. For each frequency and fixed l_S , we treat l_T as a control parameter and fit the heterostructure sheet conductance $G_{xx}^H(\omega, l_T)$ to the lin-

ear form

$$G_{xx}^H(\omega, l_T) = G_{xx,s}^H(\omega) + \sigma_{xx}^H(\omega) l_T, \quad (13)$$

which separates the thickness-independent sheet contribution $G_{xx,s}^H(\omega)$ from the bulk background $\sigma_{xx}^H(\omega)$. Note that this linear approximation is sufficient in the frequency window of interest because residual nonlinear thickness corrections are negligible [see Methods and Table S1]. Because the superconducting thickness l_S is fixed, the extrapolated sheet term $G_{xx,s}^H(\omega)$ still contains the conventional s -wave superconducting response of the parent SC [see Sec. S2 and Figs. S2(b,e)]. As shown in Fig. 4(b), the real part $\text{Re } G_{xx,s}^H(\omega)$ is strongly suppressed for $\omega < 2\Delta_{\text{ind}}$, and develops a clear, thickness-independent peak at $\omega \simeq 2\Delta_{\text{ind}}$. This feature is well separated from the broader parent s -wave gap structure appearing at $\omega = 2\Delta$. The imaginary part, $\text{Im } G_{xx,s}^H(\omega)$, combines the $1/\omega$ tail of the SC superfluid and residual Drude carriers with dispersive anomalies at these characteristic energies [Fig. 4(f)].

Using the calibrated optical responses of the standalone TI and SC slabs, we isolate the thickness-independent sheet contribution associated with the proximitized TI-SC interface. We first subtract $\frac{1}{2}G_{xx,s}^{\text{SC}}(\omega)$ and $\sigma_{xx}^{\text{SC}}(\omega) l_S$ using Eq. (12) (with $l_S = 8$ fixed), which is denoted by $G_{xx,t}^H(\omega)/G_0$, as shown in Figs. 4(c,g) [see also Figs. S2(c,f)] to remove the SC outer surface contribution and SC bulk contribution. We then remove the TI outer surface sheet response $\frac{1}{2}G_{xx,s}^{\text{TI}}(\omega)$. As shown in Figs. 4(d,h), the resulting residual interface-only

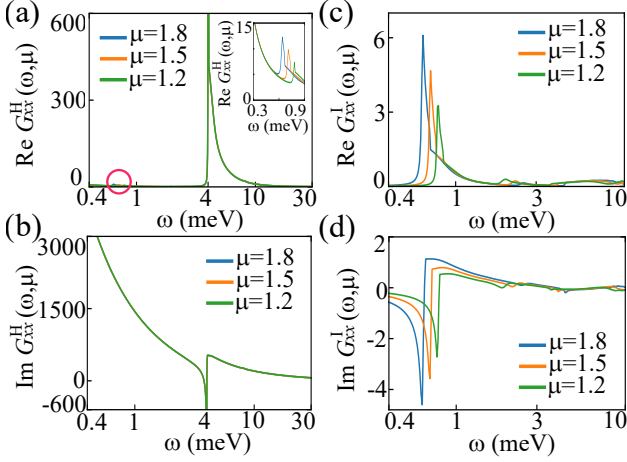


FIG. 5. **Chemical-potential dependence of the interface optical response.** (a,b) Real and imaginary parts of the total in-plane conductance $G_{xx}^H(\omega, \mu)/G_0$ for several chemical potentials μ . The dominant feature at $\omega \simeq 2\Delta$ reflects the parent s -wave condensate, while the inset in (a) resolves the additional low-energy resonance associated with the induced interface gap (red circle). (c,d) Interface-only sheet conductance $G_{xx,s}^I(\omega, \mu)/G_0$ obtained by subtracting the calibrated TI-surface and bulk-SC backgrounds from the total response. The coherence peak near $2\Delta_{\text{ind}}$ shifts and reshapes with μ , revealing the sensitivity of the induced pairing on the Dirac surface state to carrier density. All other parameters are as in Fig. 2.

sheet conductance $G_{xx}^I(\omega)$ is dominated by a sharply defined coherence peak at $\omega \simeq 2\Delta_{\text{ind}}$, which we identify as the optical fingerprint of the superconducting heterointerface. A peak near $2\Delta_{\text{ind}}$ is already visible in the raw $G_{xx}^H(\omega, l_T)$ for each l_T [Fig. 4(a) inset]. Thus, the protocol above isolates its interface-localized optical response.

This extraction procedure makes explicit that the induced-gap resonance is confined to the thickness-independent sheet channel localized at the buried interface. The pure TI slab fixes the outer-surface Dirac response, including its characteristic onset at $2|\mu|$, while the pure SC slab constrains the parent-gap feature near 2Δ together with its accompanying bulk background. Once these surface and bulk contributions are removed, the remaining interface-only sheet conductance is characterized by the single peak at $2\Delta_{\text{ind}}$. In contrast, the Drude component and broad bulk continua scale with thickness and are therefore eliminated in the extracted interfacial channel.

We further validate this interface-extraction protocol by benchmarking the interface-only sheet conductance across three complementary descriptions of the TI-SC heterointerface. As detailed in Sec. S1.3 and summarized in Fig. S1, we compare the layer-resolved interface-only sheet conductance obtained from the full TI-SC slab Hamiltonian (for $l_T = l_S = 8$) with the conductance computed from the projected interface-band subspace and with the response of the linearized 4×4 effective interfacial Hamiltonian derived via a Schrieffer-Wolff transformation. All three approaches exhibit a pronounced coherence peak at the induced-gap edge,

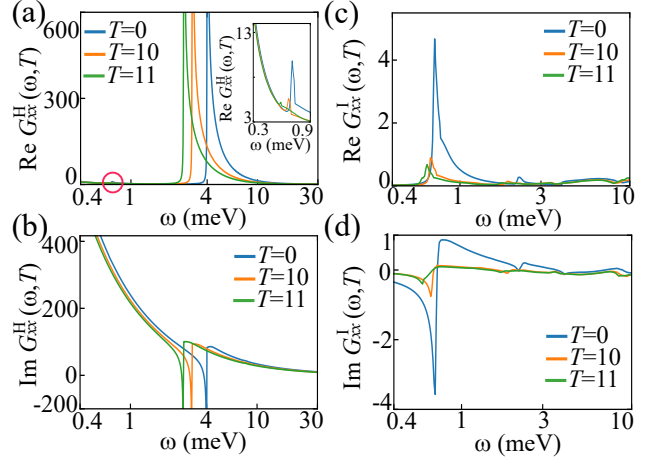


FIG. 6. **Temperature dependence of the interface optical response.** (a,b) Real and imaginary parts of the total in-plane sheet conductance $G_{xx}^H(\omega, T)/G_0$ of the TI-SC heterostructure for several temperatures T . With increasing temperature, the structure associated with the parent s -wave gap near $\omega \simeq 2\Delta$ shifts to lower energies, while the interface-induced resonance near $\omega \simeq 2\Delta_{\text{ind}}$ is progressively suppressed. The inset in (a) magnifies the induced-gap region marked by the red circle. (c,d) Interface-only sheet conductance $G_{xx,s}^I(\omega, T)/G_0$ obtained by subtracting the calibrated TI-surface and SC contributions. A single, sharp peak at $\omega \simeq 2\Delta_{\text{ind}}$ dominates the low-temperature spectra and is rapidly weakened and broadened on approaching T_c , underscoring that the interfacial coherence peak follows the superconducting order parameter while remaining at a parametrically smaller energy scale than the parent gap. All other parameters are as in Fig. 2.

$\omega = 2\Delta_{\text{ind}} = 0.71$ meV, with essentially identical peak position and closely comparable low-frequency line shape. This agreement demonstrates that the low-energy optical response is governed by the proximitized Dirac interface sector and that our procedure faithfully isolates the corresponding sheet contribution. At higher frequencies, the linearized effective theory displays the nearly constant Dirac-continuum background $e^2/16\hbar$, whereas, the full heterostructure redistributes part of this spectral weight over a broader energy range through contributions from bands and virtual processes not retained in the leading-order Schrieffer-Wolff reduction. Consistently, the conductance computed from the projected interface-bands subspace reproduces the same qualitative low-frequency features of the layer-resolved slab result, providing an independent validation of the extrapolated interface-only sheet conductance used in Eq. (13).

In realistic superconducting films, disorder and defects yield a finite quasiparticle lifetime and inhomogeneous broadening. These effects smear the clean-limit BCS threshold singularity at $\omega = 2\Delta$ and turn it into a broadened absorption edge. This evolution from the high-purity to the dirty limit is captured by the arbitrary-purity optical conductivity of Zimermann *et al.* [37]. It is also consistent with THz measurements on disordered superconducting films such as NbN [38]. We nevertheless adopt a clean SC slab with minimal broaden-

ing as a controlled reference baseline. This choice isolates the intrinsic BCS pair-breaking line shape and provides a transparent calibration of the bulk superconducting contribution that we later subtract in the interface-extraction protocol. The thickness-extrapolation and subtraction procedure does not require a sharp and resolvable 2Δ cusp. Disorder mainly broadens the intrinsic BCS threshold feature [37]. The interface isolation remains valid when the SC films are sufficiently homogeneous. In that case, $G_{xx}(\omega, l)$ is well approximated by a thickness-independent sheet term plus a bulk term that is linear in l .

We now investigate how the optical response of the proximity-induced superconducting state at the TI-SC interface can be tuned by the chemical potential and temperature. Figures 5 and 6 summarize the evolution of both the total sheet conductance and the conductance spectrum isolated to the interfacial channel. Varying the chemical potential μ modifies the Fermi surface of the Dirac cone formed at the TI-SC interface and shifts the Dirac threshold $2|\mu|$, which sets the onset of interband absorption associated with the TI surface state. In the total sheet conductance, this appears as a redistribution of spectral weight between the Drude contribution and the interband absorption [Figs. 5(a,b)]. By contrast, when we focus on the interface channel alone, the coherence peak near $\omega \simeq 2\Delta_{\text{ind}}$, corresponding to the induced superconducting gap Δ_{ind} , shifts in frequency and changes shape as a function of μ [Figs. 5(c,d)]. This evolution is consistent with a proximitized Dirac band whose Fermi level is tuned relative to both the induced gap and the parent superconducting energy scale 2Δ .

We now examine how the optical response of the proximity-induced superconducting state at the TI-SC interface evolves with temperature. Figure 6 illustrates how the optical response of the interfacial superconducting state in the TI-SC heterostructure evolves with temperature. In Figs. 6(a,b), the total complex conductance $G_{xx}^H(\omega, T)$ shows that, as the temperature increases, the structure associated with the parent s -wave gap near $\omega \simeq 2\Delta$ gradually shifts to lower energies, while the low-frequency magnitude of $\text{Im } \sigma_{xx}(\omega, T)$, which reflects the superfluid response, is strongly reduced. Consistently, the interface-only conductance $G_{xx}^I(\omega, T)$ displayed in Figs. 6(c,d) exhibits a sharp interfacial coherence peak at $\omega \simeq 2\Delta_{\text{ind}}$ at low temperatures whose height decreases and whose width broadens with increasing temperature, eventually rendering the peak nearly invisible as the system approaches T_c . This behavior visually demonstrates that the resonance observed at the interface faithfully tracks the suppression of the parent superconducting order parameter while remaining confined to a smaller, well-separated energy scale characteristic of the interface-induced superconducting response.

Figure 7 summarizes the evolution of the parent and induced superconducting energy scales as functions of chemical potential and temperature. In Fig. 7(a), we plot the characteristic frequencies $\omega_{\text{SC}}(\mu)$ and $\omega_{\text{ind}}(\mu)$, extracted from the peak positions of $\text{Re } G_{xx}^H(\omega, \mu)$ and corresponding to the bulk su-

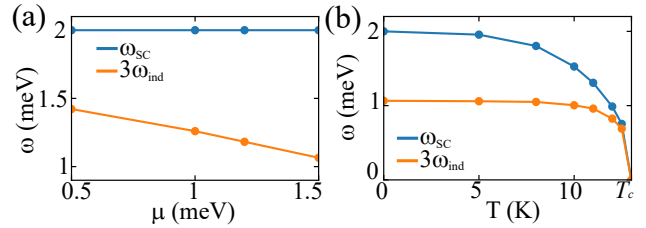


FIG. 7. **Evolution of the parent and induced superconducting energy scales with chemical potential and temperature.** (a) Characteristic frequencies $\omega_{\text{SC}}(\mu)$ and $3\omega_{\text{ind}}(\mu)$ obtained from the peak positions of $\text{Re } G_{xx}^H(\omega, \mu)$, representing the parent superconducting gap and the induced TI-SC interface gap, respectively, as functions of chemical potential. (b) Same analysis as a function of temperature at fixed μ , showing $\omega_{\text{SC}}(T)$ and $3\omega_{\text{ind}}(T)$ extracted from $\text{Re } G_{xx}^H(\omega, T)$. The two panels highlight that the induced interfacial scale is tunable and remains well separated from the parent superconducting scale while collapsing near T_c . All other parameters are as in Fig. 2.

perconducting gap of the parent SC and the induced TI-SC interface gap, respectively. For clarity, the induced-gap curve is shown as $3\omega_{\text{ind}}(\mu)$. While the parent-gap scale $\omega_{\text{SC}}(\mu)$ remains essentially independent of μ over the range considered, the induced-gap frequency exhibits a pronounced dependence on μ , reflecting the sensitivity of the proximity pairing on the Dirac surface state to the carrier density and band alignment at the interface.

In Fig. 7(b), we perform the same analysis as a function of temperature, displaying $\omega_{\text{SC}}(T)$ and $3\omega_{\text{ind}}(T)$ obtained from $\text{Re } G_{xx}^H(\omega, T)$ at fixed μ . Both the parent and induced energy scales decrease monotonically with increasing temperature and vanish near the critical temperature T_c . This behavior demonstrates that the coherence peak associated with the interface gap follows the temperature dependence of the parent superconducting order parameter, while remaining at a smaller, well-separated energy scale characteristic of the induced proximity gap.

Taken together, Figs. 3-7 establish a coherent picture of the proximity-induced superconducting state at the TI-SC interface. The optical sheet conductance enables us to disentangle bulk and surface contributions, isolate the Dirac surface-sheet response as a genuinely two-dimensional channel, and track the opening of an induced gap that is clearly distinct from the parent superconducting gap. The evolution of the corresponding energy scales with chemical potential and temperature shows that the induced gap is both tunable by carrier density and locked to the parent order parameter through its temperature dependence, vanishing at the same critical temperature. These results demonstrate that terahertz spectroscopy can resolve the hierarchy of superconducting energy scales in TI-SC heterostructures and provide a noninvasive, bulk-compatible probe of buried topological superconducting interfaces that is complementary to conventional surface-sensitive techniques.

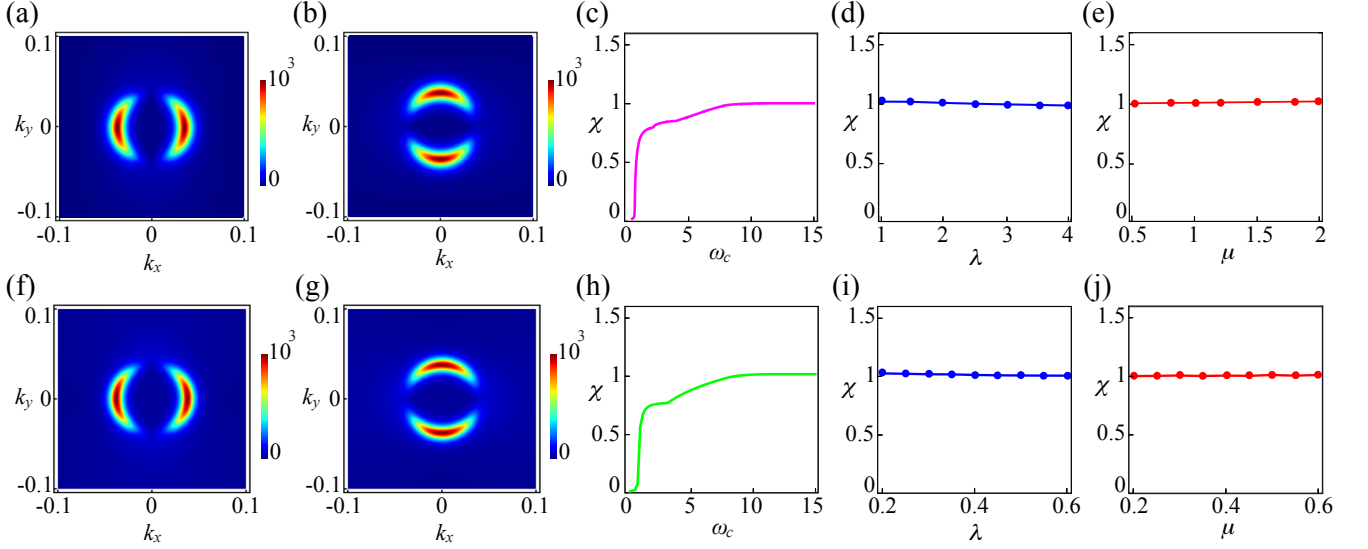


FIG. 8. Quantum metric and optical sum rule at the TI-SC interface. (a-e) Full TI-SC heterostructure results from the projected interface-bands subspace. (a,b) Quantum-metric components $g_{xx}(\mathbf{k})$ and $g_{yy}(\mathbf{k})$, strongly enhanced on the minimal-gap ring of the proximitized Dirac interface. (c) Optics-geometry ratio $\chi(\omega_c)$ [Eq. (16)] obtained from the interface-only sheet conductance $G_{xx}(\omega)$ and the quantum-metric integral over the projected interface-bands subspace. $\chi(\omega_c)$ rises sharply at the induced-gap coherence peak $\omega = 2\Delta_{\text{ind}} \simeq 0.71$ meV and saturates to $\chi \simeq 1$ at higher cutoff. (d,e) χ versus proximity coupling λ and chemical potential μ , evaluated over $\mathcal{R} : (k_x, k_y) \in [-0.1, 0.1] \times [-0.1, 0.1]$, showing $\chi \simeq 1$ across moderate parameter variations. In (d) λ is varied keeping μ fixed at 1.5 meV and in (e) μ is varied with proximity coupling $\lambda = 3$. (f-j) Schrieffer-Wolff effective interfacial BdG theory. (f,g) Quantum-metric maps exhibiting the same minimal-gap-ring enhancement as in (a,b). (h) $\chi(\omega_c)$ computed fully within the effective theory, reproducing the onset at $2\Delta_{\text{ind}}$ and saturation to $\chi \simeq 1$ in (c). (i,j) χ versus λ and μ over the same region \mathcal{R} , remaining close to unity. In (i) λ is varied keeping μ fixed at 0.6 meV and in (j) μ is varied with a fixed $\lambda = 0.6$. All other model parameters are the same as in Fig. 2.

Quantum Geometry from the Optical Response

Having established that the interface sheet conductance exhibits a sharp coherence peak at photon energy $\omega = 2\Delta_{\text{ind}}$, we now turn to its microscopic origin. We show that this resonance is governed by the quantum geometry of the proximitized Dirac surface state and that its low-frequency optical spectral weight provides a direct probe of the quantum metric of the emergent two-dimensional TSC at the heterointerface.

In a generic gapped multiband system, the linear-response optical conductivity/conductance is controlled not only by band dispersion but also by the underlying quantum geometry of the Bloch (or BdG) bands, encoded in the quantum metric. For the effective two-dimensional interface Hamiltonian in Eq. (6), we characterize this geometry by the quantum weight $K_{\mu\nu}$, defined as the Brillouin-zone integral of the quantum metric $g_{\mu\nu}(\mathbf{k})$. Following Ref. [32], $K_{\mu\nu} = 2\pi \int_{BZ} \frac{d^2\mathbf{k}}{4\pi^2} g_{\mu\nu}(\mathbf{k})$ coincides with the quadratic (q^2) coefficient in the small-wave-vector expansion of the static structure factor and thus provides a geometric measure of the spatial fluctuations of the superconducting ground state. The quantum metric is given by [39]

$$g_{\mu\nu}(\mathbf{k}) = \frac{1}{2} \text{Tr}[\partial_\mu P(\mathbf{k}) \partial_\nu P(\mathbf{k})], \quad (14)$$

where $P(\mathbf{k}) = \sum_{E_n(\mathbf{k}) < 0} |u_n(\mathbf{k})\rangle \langle u_n(\mathbf{k})|$ is the projector onto the occupied Bogoliubov quasiparticle subspace and

$|u_n(\mathbf{k})\rangle$ is the n th normalized eigenvector of the BdG Hamiltonian.

The connection to the optical response follows from the fluctuation-dissipation relation between equal-time density correlations and the frequency-integrated dynamical structure factor, which constrains the longitudinal optical conductivity/conductance in terms of the quantum metric [32, 34, 40, 41]. Specialized to the longitudinal interface-only sheet conductance $G_{\mu\mu}(\omega)$, this yields the sum rule for the longitudinal optical response [32],

$$\int_{0+}^{\infty} d\omega \frac{\text{Re} G_{\mu\mu}(\omega)}{\omega} = \frac{\pi e^2}{h} K_{\mu\mu}. \quad (15)$$

Thus, the negative-first moment of the optical conductance is a purely geometric quantity, fixed by the integrated quantum metric of the occupied interface bands.

In what follows, we evaluate this optics-geometry correspondence in two complementary descriptions of the TI-SC interface. We first extract the interfacial quantum metric and sheet conductance from the full TI-SC slab by constructing a projected low-energy interface-bands subspace. We then compute the same quantities within the Schrieffer-Wolff low-energy effective interfacial BdG Hamiltonian. Their agreement provides a stringent validation that the optical resonance directly reflects the interfacial quantum metric.

In our TI-SC heterostructure, superconducting proximity opens an induced gap in the Dirac surface state, thereby en-

dowing the interfacial bands with a nontrivial quantum geometry. To access the interfacial sector directly from the full TI-SC slab, we construct a low-energy interface subspace by projecting the slab eigenstates onto the heterointerface degrees of freedom, which yields a set of interface bands that faithfully encode the proximitized Dirac physics. Figs. 8(a,b) report the momentum-resolved quantum-metric components $g_{xx}(\mathbf{k})$ and $g_{yy}(\mathbf{k})$ evaluated within this projected interface-band subspace. The metric exhibits pronounced hot spots on a closed ring in \mathbf{k} -space where the direct BdG quasiparticle gap is minimal, identifying the gap-edge manifold that dominates the interfacial quantum geometry. This ring-like enhancement reflects the generic inverse-squared gap dependence of the quantum metric and the concomitant rapid variation of occupied and unoccupied eigenstates near a proximity-induced avoided crossing. Because the quantum metric is sharply concentrated near the minimal-gap ring, we evaluate the quantum-metric weight within a low-energy momentum window \mathcal{R} that encloses this ring, which captures the dominant interfacial contribution relevant for low-frequency optics.

We next quantify how this interfacial quantum geometry is encoded in the optical response through a generalized optical sum rule. On the optical side, we extract the interface-only sheet conductance $G_{xx}(\omega)$ from the layer-resolved spectrum of the full TI-SC slab, thereby isolating the thickness-independent interfacial contribution. On the geometric side, we define a partial quantum weight by integrating $g_{xx}(\mathbf{k})$ over \mathcal{R} that encloses the minimal-gap ring. We then introduce the dimensionless optics-geometry ratio $\chi(\omega_c)$, defined as the partial optical sum rule $\int_{0+}^{\omega_c} d\omega \text{Re } G_{xx}(\omega)/\omega$ normalized by the quantum-metric integral over \mathcal{R} ,

$$\chi(\omega_c) = \left[\int_{0+}^{\omega_c} d\omega \frac{\text{Re } G_{xx}(\omega)}{\omega} \right] \bigg/ \left[\frac{e^2}{2h} \int_{\mathcal{R}} d^2\mathbf{k} g_{xx}(\mathbf{k}) \right]. \quad (16)$$

By construction, $\chi(\omega_c) \simeq 1$ signals that the low-frequency optical integral has saturated the quantum-metric weight contained in \mathcal{R} . Figure 8(c) shows that $\chi(\omega_c)$ increases sharply as the cutoff crosses the induced-gap coherence peak at $\omega = 2\Delta_{\text{ind}} \simeq 0.71$ meV, indicating that the dominant fraction of the interfacial quantum weight is already captured by the low-frequency optical spectral weight associated with proximity-induced gap opening. With increasing cutoff, $\chi(\omega_c)$ approaches $\chi \simeq 1$, demonstrating saturation of the generalized optical sum rule within the chosen low-energy momentum window.

Crucially, this optics-quantum geometry correspondence is not an artifact of the projection procedure but is reproduced quantitatively by a controlled low-energy description. Figures 8(f,g) show the quantum-metric maps computed from the Schrieffer-Wolff (SW) effective interfacial BdG Hamiltonian, which exhibit the same minimal-gap-ring enhancement as the full-system results in Figs. 8(a,b). This agreement establishes that the SW reduction faithfully captures the interfacial quantum geometry encoded by the full TI-SC heterostructure. Consistently, Fig. 8(h) evaluates $\chi(\omega_c)$ entirely within

the SW framework, with both $g_{xx}(\mathbf{k})$ and $G_{xx}(\omega)$ computed self-consistently from the same effective Hamiltonian, and finds the same rapid onset near $2\Delta_{\text{ind}}$ and saturation towards $\chi \simeq 1$ as in Fig. 8(c). Taken together, Figs. 8(a-c,f-h) demonstrate that a low-frequency integral of the generalized optical weight provides an experimentally accessible and quantitatively controlled probe of the interfacial quantum weight. Because the negative-first moment $\int d\omega \text{Re } G_{xx}(\omega)/\omega$ amplifies low-frequency contributions, it is particularly sensitive to proximity-driven changes of the ground-state wavefunction and therefore well suited for detecting emergent quantum geometry across interfacial topological transitions.

Finally, Figs. 8(d,e) shows that the saturation of χ remains robust under moderate variations of the proximity-coupling strength λ and the chemical potential μ in the full TI-SC system. The same robustness is reproduced within the SW theory in Figs. 8(i,j), even though changing λ and μ renormalizes the dressed low-energy parameters of the effective model. The persistence of $\chi \simeq 1$ across both descriptions establishes that the optical sum rule-quantum metric correspondence is a generic low-energy property of the proximitized Dirac interface sector rather than a fine-tuned feature of a particular parameter set.

Consequently, integrating the interfacial generalized optical weight up to a cutoff that covers the induced-gap coherence peak provides a controlled lower bound that rapidly approaches the full quantum-metric weight contained in \mathcal{R} .

DISCUSSION

Model Considerations and Generality

The layered TI-SC slab model we employ is designed to retain only the minimal microscopic ingredients required for proximity-induced superconductivity at a topological interface, while remaining anchored to realistic materials. The TI block reproduces the band inversion of the canonical four-band model of Bi_2Se_3 within a lattice regularization [42, 43]. The bulk gap is intentionally reduced to enhance the numerical visibility of proximity-induced optical features, while keeping the \mathbb{Z}_2 topological class unchanged. The superconducting block is chosen to represent a metallic band with a bandwidth of several hundred meV and a pairing amplitude in the meV range, consistent with Nb-based thin films at low temperature. The interface hopping is chosen such that $\Delta_{\text{ind}} \ll \Delta$ yet clearly resolvable, corresponding to an intermediate-proximity regime where the Dirac cone remains surface-localized and helical. By tuning the chemical potential close to the Dirac point, we emulate gated or compensated Bi_2Se_3 or Bi_2Te_3 samples in which bulk carriers are strongly suppressed, a regime that has been realized in several experiments.

Experimental prospects and Thickness Protocol

The frequency scales and signal strengths we find are compatible with state-of-the-art terahertz and infrared spectroscopies, which have already been deployed on TI-SC heterostructures [25–27]. For $\text{Bi}_2\text{Se}_3\text{-Nb}$ or $\text{Bi}_2\text{Te}_3\text{-Pb}$ interfaces, induced gaps of order 1–3 meV fall in the terahertz regime, implying that the coherence peak at $\omega = 2\Delta_{\text{ind}}$ could be observable as a pronounced feature in the real part of the optical response or in reflectivity. Our calculations predict that this induced-gap resonance appears as a thickness-independent contribution to the in-plane sheet conductance, superimposed on a thickness-dependent Drude and interband background arising from bulk carriers. A characteristic temperature dependence of this peak—following the opening and closing of the induced gap—would provide a clear spectroscopic hallmark of interfacial superconductivity in a buried topological layer. In practice, $G_{xx}(\omega)$ can be extracted by fitting thin-film Fresnel/transfer-matrix models to the measured complex transmission (or reflectivity) in time-domain terahertz and infrared ellipsometry.

To access this interface signal in practice, we propose a thickness-extrapolation protocol in which the topological-insulator thickness l is used as a control parameter. For a series of heterostructures with identical materials, disorder levels, and chemical potential, but varying l_T , one measures the complex sheet conductance $G_{xx}(\omega, l_T)$ using time-domain terahertz spectroscopy or broadband infrared ellipsometry at fixed (μ, T) . At each frequency ω , the l_T -dependence of the measured conductance can then be decomposed into a thickness-independent sheet term, dominated by surfaces and interfaces, and a thickness-dependent bulk background. For a pure topological-insulator series, this procedure yields the combined sheet response of the top and bottom surfaces. For a matched TI-SC series, the extracted sheet term contains both the exposed TI and SC surfaces as well as the buried TI-SC interface. Subtracting the calibrated single-surface baseline, determined from both the pure-TI and pure-SC series, isolates the interface-only spectrum of the heterostructure. An analogous analysis of the low-frequency Drude response enables the determination of both the interface superfluid stiffness and residual quasiparticle weight on the same footing.

Limitations and Outlook

Our analysis relies on a number of simplifying assumptions that delineate the regime of validity of the proposed protocol and point towards future extensions. We work in a clean, translationally invariant slab geometry, neglecting disorder, interface roughness, and inhomogeneous strain, all of which can broaden the coherence peak and partially mix surface and bulk optical channels. We also approximate the superconducting layer by a single-band, mean-field BCS description and ignore strong-coupling effects, multi-gap physics, and quasiparticle renormalizations that may be relevant in specific ma-

terial combinations. In addition, we focus on linear-response optics and do not address non-equilibrium phenomena such as pump-probe dynamics, photo-induced superconductivity, or nonlinear optical probes of topology. A systematic treatment of these effects, for example by incorporating realistic disorder profiles, multiorbital first-principles input, or time-dependent Bogoliubov-de Gennes simulations, is an important direction for future work.

On the experimental side, successful implementation of the thickness-extrapolation protocol requires precise control over film thickness, chemical potential, and interface quality across the entire sample series, as well as accurate phase-sensitive measurements of the complex sheet conductance. In practice, extracting $G_{xx}(\omega)$ from experiment entails fitting thin-film Fresnel/transfer-matrix models to the measured complex transmission in time-domain terahertz spectroscopy and infrared ellipsometry, so that systematic uncertainties from multilayer optics, substrate response, and thickness calibration must be carefully controlled. Nevertheless, the required ingredients lie well within current capabilities of molecular-beam epitaxy, van der Waals assembly, and terahertz time-domain spectroscopy. Further, in Sec. S4 we discuss the optical conductivity of the helical Majorana boundary modes present in our model, using an effective one-dimensional edge Hamiltonian [44]. A numerical simulation of the optical properties of these boundary modes arising in a mixed parity topological superconductor would be an interesting extension of our study and could provide valuable insights into designing experiments to detect signatures of the elusive Majorana fermion.

Looking ahead, it will be interesting to extend the present approach to platforms where topological superconductivity emerges from more complex band structures, such as higher-order TIs, moiré systems with flat bands, or strongly correlated quantum anomalous Hall insulators. In such settings, the combination of spatially resolved optics, thickness extrapolation, and quantum-geometric sum rules may provide a powerful toolkit for characterizing both the superconducting order and the underlying band topology, and for guiding the design of future devices for topological quantum information processing.

CONCLUSION

Our work demonstrates that a TI-SC heterostructure can realize a two-dimensional, proximity-induced topological superconducting state at a buried interface, and that this is spectroscopically accessible through the interface sheet conductance. By combining Kubo formalism with thickness scaling to separate bulk and sheet channels, we isolate an interface-only optical response whose dominant low-frequency resonance is tied to the induced superconducting gap of the proximitized Dirac surface sector, rather than to bulk TI or bulk SC contributions. Moreover, this interface conductance is quantitatively governed by a quantum-metric sum rule. The

negative-first moment of the optical response directly measures the proximity-induced quantum weight of the gapped Dirac surface state. These findings identify a conceptually new optical route to diagnosing emergent topological superconductivity and Majorana-compatible physics in TI-SC heterostructures, thereby complementing and extending transport-based approaches.

The present results motivate several experimental directions. Terahertz time-domain spectroscopy and infrared measurements on TI-SC thin-film series with systematically varied TI thickness are expected to reveal a thickness-independent conductance resonance at the induced interfacial gap scale, thereby testing whether the superconducting optical resonance is of buried-interface origin rather than a bulk contribution [45]. More broadly, magnetic-field tuning provides a complementary probe of the Majorana sector. Controlled time-reversal-symmetry breaking can split or gap the low-energy spectrum, enabling systematic studies of Majorana hybridization and its controllability [3–7].

METHODS

Model System Analysis

To describe the low-energy electronic structure of the TI surface, we start from the linearized Dirac Hamiltonian expanded about the bulk gap-closing point at Γ [46], which captures the band inversion and spin-momentum locking of a three-dimensional TI. This linearized Hamiltonian of the TI is split into the Dirac equation section H_{TI}^D and the perturbation section H_{TI}^P , which are

$$\begin{aligned} H_{\text{TI}}^D &= M\tau_z - i\alpha\tau_x\sigma_z\partial_z, \\ H_{\text{TI}}^P &= -\mu\tau_0 + \alpha\tau_x(k_x\sigma_x + k_y\sigma_y), \end{aligned}$$

where τ_i and σ_i are Pauli matrices acting in orbital and spin space, respectively, and $M = m_0 + 3t_0$ sets the bulk Dirac mass at the Γ point. The Fermi velocity of the Dirac cone is given as α . The chemical potential μ is measured relative to the bulk band inversion and is chosen such that the Fermi level lies in the vicinity of the surface Dirac cone in the heterostructure.

The surface modes are obtained by solving the Dirac part H_{TI}^D with a spatially varying mass $M(z)$ that changes sign across the TI-vacuum boundary. This reduces to a Jackiw-Rebbi problem, and yields exponentially localized eigenstates at the TI surface [47, 48]. Projecting the perturbation Hamiltonian H_{TI}^P onto the subspace spanned by these Jackiw-Rebbi solutions leads to an effective two-dimensional surface Dirac Hamiltonian with Fermi velocity α and chemical potential μ , as summarized in Sec. S1.1.

The superconducting slab is described by a minimal s -wave BdG model that is periodic in-plane and finite along the surface normal, and we focus on the interfacial degrees of freedom relevant for proximity coupling to the TI surface sector.

Unlike the TI, the parent SC does not host a topological surface Dirac mode; hence, its impact on the low-energy surface response arises mainly through hybridization with the TI surface bands at the heterointerface. To model this hybridization, we introduce a local tunneling Hamiltonian between TI and SC electrons,

$$H_{\text{I}} = \sum_{j,s} \lambda \left(a_{j,s}^\dagger c_{j,s} + c_{j,s}^\dagger a_{j,s} \right),$$

where $a_{j,s}$ and $c_{j,s}$ are the annihilation operators for the electrons of the SC and TI for spin s at site j , respectively. By applying the Schrieffer–Wolff transformation with the TI surface sector as the low-energy subspace and the coupled SC states as virtual high-energy excitations, we obtain the dressed TI surface Hamiltonian in Eq. (6). It incorporates an induced pairing term and a renormalized Dirac velocity, serving as a minimal effective model for the proximitized surface[see more details in Sec. S1.2].

Using the Jackiw-Rebbi solutions, we find the edge Hamiltonians of the heterointerface Hamiltonian [46],

$$H_x^{\text{edge}}(k_x) = -k_x(\alpha\xi_y + \Delta_p\xi_x), \quad (17)$$

$$H_y^{\text{edge}}(k_y) = k_y(\alpha\xi_y + \Delta_p\xi_x), \quad (18)$$

where $H_i^{\text{edge}}(k_i)$ describes the edge along direction $i = x, y$ with conserved momentum k_i , and $\xi_{x,y}$ are Pauli matrices acting in the effective edge (Nambu or Majorana) pseudospin space. The resulting zero-energy states of the edge Hamiltonians of Eqs. (17) and (18) are the Majorana edge states given in Eq. (9) [see more details in Sec. S1.2].

Optical Response of Slab Geometries

The in-plane optical response of the TI slabs, SC slabs, and TI-SC heterostructures is computed within a unified linear-response framework using a slab Hamiltonian $H_{\text{slab}}(\mathbf{k})$ that is periodic in the (x, y) directions and open along z . For each in-plane momentum $\mathbf{k} = (k_x, k_y)$, we diagonalize the normal or BdG slab Hamiltonian,

$$H_{\text{slab}}(\mathbf{k})|\psi_{n\mathbf{k}}\rangle = E_{n\mathbf{k}}|\psi_{n\mathbf{k}}\rangle, \quad (19)$$

with eigenstates normalized over the two-dimensional Brillouin zone. This two-dimensional normalization implies that the current operator extracted from H_{slab} naturally describes a current per unit length and thus yields a sheet conductance rather than a bulk conductivity.

The in-plane velocity operator is defined by the k -derivative of the slab Hamiltonian,

$$v_x(\mathbf{k}) = \frac{1}{\hbar}\partial_{k_x}H_{\text{slab}}(\mathbf{k}), \quad (20)$$

and the corresponding current operator is

$$\hat{J}_x^{\text{2D}}(\mathbf{k}) = -ev_x(\mathbf{k}). \quad (21)$$

Because $H_{\text{slab}}(\mathbf{k})$ is normalized per unit area, \hat{J}_x^{2D} transports charge per unit length, in contrast to the three-dimensional current density (A/m^2) that appears in bulk Kubo formulae. The linear-response kernel constructed from \hat{J}_x^{2D} therefore has units $[G_{xx}] = \frac{\text{A/m}}{\text{V/m}} = \text{S}$, and we interpret $G_{xx}(\omega, l)$ as the in-plane sheet conductance of a slab of thickness l .

In the eigenbasis $\{|\psi_{n\mathbf{k}}\rangle\}$, the interband part of the longitudinal sheet conductance, $G_{xx}^{\text{Int}}(\omega, l)$, takes the standard form

$$G_{xx}^{\text{Int}}(\omega, l) = \frac{i}{N_k} \sum_{\mathbf{k}} \sum_{m \neq n} \frac{f_{n\mathbf{k}} - f_{m\mathbf{k}}}{\Omega_{mn}(\mathbf{k})} \frac{|\langle \psi_{n\mathbf{k}} | \hat{J}_x^{\text{2D}} | \psi_{m\mathbf{k}} \rangle|^2}{\omega + i\eta - \Omega_{mn}(\mathbf{k})}, \quad (22)$$

where $\Omega_{mn}(\mathbf{k}) = E_{m\mathbf{k}} - E_{n\mathbf{k}}$, $f_{n\mathbf{k}}$ is the Fermi function, N_k is the number of \mathbf{k} -points, and η is a small phenomenological broadening. For uniform \mathbf{k} meshes, $(1/N_k) \sum_{\mathbf{k}}$ approximates the Brillouin-zone average. No explicit factor of l appears in this expression, since the current operator is already defined per unit length. Any residual thickness dependence of $G_{xx}(\omega, l)$ therefore reflects a redistribution of spectral weight between surface-like and bulk-like layers rather than a change in the dimensionality of the response. We evaluate the retarded response by the prescription $\omega \rightarrow \omega + i\eta$, and $\text{Re } G_{xx}(\omega)$ reported in the main text refers to the regular (finite-frequency) absorption, with the $\omega = 0$ singular contribution encoded separately in the Drude term.

The full complex sheet conductance is written as

$$G_{xx}(\omega, l) = G_{xx}^{\text{D}}(\omega, l) + G_{xx}^{\text{Int}}(\omega, l), \quad (23)$$

where $G_{xx}^{\text{D}}(\omega, l) = iD_{xx}(l)/(\omega + i\eta)$ is the Drude contribution characterized by a slab-thickness-dependent Drude weight $D_{xx}(l)$, and G_{xx}^{Int} is the interband contribution. In the superconducting (BdG) case, we avoid double counting of particle-hole degrees of freedom by including the standard overall factor of $1/2$ in the current-current response kernel. Throughout we report $G_{xx}(\omega, l)$ in units of the conductance quantum $G_0 = e^2/h$.

All calculations are converged with respect to the number of \mathbf{k} -points and the frequency sampling. We use uniform meshes in the two-dimensional Brillouin zone with up to $\mathcal{O}(10^4)$ \mathbf{k} -points and choose η and T to match the values used in the main-text figures, thereby mimicking realistic disorder and finite-temperature broadening.

To separate bulk, surface, and interface contributions to the optical response, we exploit the real-space structure of the slab eigenstates. For each eigenstate $|\psi_{n\mathbf{k}}\rangle$, we compute the probability weight on every atomic layer along z and group these layers into predefined regions, top TI, bottom SC surfaces, TI bulk, interface layers, and SC bulk. The corresponding region projectors are then used to reweight the Kubo kernel and generate channel-resolved sheet conductances, such as surface-surface, surface-bulk, and interface-interface responses, which is consistent with the layer-resolved analysis below.

Layer-Resolved Analysis

To separate surface and interface responses from bulk contributions, we analyze the thickness scaling of the sheet conductance and obtain the thickness-independent term by extrapolation. For each (μ, T, η) and frequency ω , we compute the longitudinal sheet conductance $G_{xx}(\omega, l)$ for a series of slab thicknesses l and fit it to a low-order polynomial,

$$G_{xx}(\omega, l) = G_{xx,s}(\omega) + \sigma_{xx}(\omega) l + c(\omega) l^2, \quad (24)$$

where $G_{xx,s}(\omega)$ is the thickness-independent sheet contribution dominated by surfaces and interfaces, $\sigma_{xx}(\omega)$ is an effective bulk conductivity setting the linear background, and $c(\omega)$ captures weak nonlinearities in l due to finite-size and boundary effects. At each frequency ω , we perform an independent fit over the thickness series used in the figure calculations. In practice, $c(\omega)$ is found to be negligible over the frequency range of interest, and a purely linear form $G_{xx}(\omega, l) \simeq G_{xx,s}(\omega) + \sigma_{xx}(\omega)l$ is sufficient in this work [see the representative fitting parameters in Table S1].

For pure TI slabs, we apply Eq. (24) to the TI sheet conductance $G_{xx}^{\text{TI}}(\omega, l_T)$,

$$G_{xx}^{\text{TI}}(\omega, l_T) = G_{xx,s}^{\text{TI}}(\omega) + \sigma_{xx}^{\text{TI}}(\omega) l_T + c^{\text{TI}}(\omega) l_T^2, \quad (25)$$

where l_T is the TI thickness, $G_{xx,s}^{\text{TI}}(\omega)$ denotes the combined sheet conductance of the two TI surfaces, and $\sigma_{xx}^{\text{TI}}(\omega)$ is the effective TI bulk conductivity. Since there are two surfaces (top and bottom) for a pure TI slab, the single TI surface sheet conductance is identified as

$$G_{xx,\text{single}}^{\text{TI}}(\omega) = \frac{1}{2} G_{xx,s}^{\text{TI}}(\omega). \quad (26)$$

The sheet conductance extracted from the thickness series agrees quantitatively with the surface-only channel obtained from the layer projectors, providing an internal consistency check of the extrapolation procedure [see Figs. 3(b,c,e,f)].

For pure SC slabs, we perform an analogous analysis by varying the SC thickness l_S and fitting

$$G_{xx}^{\text{SC}}(\omega, l_S) = G_{xx,s}^{\text{SC}}(\omega) + \sigma_{xx}^{\text{SC}}(\omega) l_S + c^{\text{SC}}(\omega) l_S^2, \quad (27)$$

where $G_{xx,s}^{\text{SC}}(\omega)$ captures the thickness-independent sheet response of the two SC surfaces and $\sigma_{xx}^{\text{SC}}(\omega)$ is the SC bulk conductivity [see Fig. S2 in Sec. S2]. The single SC surface sheet conductance is then identified as

$$G_{xx,\text{single}}^{\text{SC}}(\omega) = \frac{1}{2} G_{xx,s}^{\text{SC}}(\omega). \quad (28)$$

In practice, both $c^{\text{TI}}(\omega)$ and $c^{\text{SC}}(\omega)$ are negligible, ensuring that the purely linear form is sufficient [see Table S1].

For TI-SC heterostructures, we fix the SC thickness l_S , vary the TI thickness l_T , and fit

$$G_{xx}^{\text{H}}(\omega, l_T) = G_{xx,s}^{\text{H}}(\omega) + \sigma_{xx}^{\text{H}}(\omega) l_T + c^{\text{H}}(\omega) l_T^2, \quad (29)$$

to obtain the total thickness-independent sheet term $G_{xx,s}^{\text{H}}(\omega)$ and the effective bulk background $\sigma_{xx}^{\text{H}}(\omega)$ at each frequency.

At fixed l_S , $G_{xx}^H(\omega)$ contains three contributions, the outer TI surface, the buried TI-SC interface, and the outer SC surface term that are independent of l_T . The outer TI surface is calibrated using the pure TI series via Eq. (26), while the SC surface and bulk contributions are obtained from the pure SC series via Eqs. (27). Subtracting these baselines isolates the interface's spectrum,

$$G_{xx}^I(\omega) \simeq G_{xx,s}^H(\omega) - G_{xx,\text{single}}^{\text{TI}}(\omega) - G_{xx,\text{single}}^{\text{SC}}(\omega) - \sigma_{xx}^{\text{SC}}(\omega)l_S, \quad (30)$$

which is the quantity plotted as the interface sheet conductance in Figs. 4-6. The approximation in Eq. (30) reflects that we fix l_S in the heterostructure series and treat the residual SC response as the calibrated single-surface term plus the bulk background $\sigma_{xx}^{\text{SC}}(\omega)l_S$.

The same logic applies to the low-frequency Drude response. By fitting the Drude weight, or equivalently the zero-frequency limit of $\omega \text{Im } G_{xx}(\omega, l)$, as a function of l , a bulk contribution that scales with thickness l , can be separated from a thickness-independent surface or interface Drude term.

Note that the sheet conductance extracted from the thickness series agrees quantitatively with the surface-only channel obtained from the layer projectors, providing an internal consistency check of the extrapolation procedure.

ACKNOWLEDGMENTS

This work was supported by the National Research Foundation of Korea (NRF) funded by the Ministry of Science and ICT (MSIT), South Korea (Grants No. NRF-2022R1A2C1011646, RS-2024-00416036, and RS-2025-03392969). This work was supported by Creation of the Quantum Information Science R&D Ecosystem (Grant No. RS-2023-NR068116) through the NRF funded by the Korean government (MSIT). This work was supported by the Quantum Simulator Development Project for Materials Innovation through the NRF funded by the MSIT, South Korea (Grant No. RS-2023-NR119931). This work was also supported by Brain Pool program funded by the Ministry of Science and ICT through the National Research Foundation of Korea (Grant No. RS-2025-25446099). J. H. Kim was supported by the Samsung Science and Technology Foundation (Grant No. SSTF-BA2102-04).

AUTHOR CONTRIBUTIONS

M. Kang, Y. Prasad, and N. D. Babu equally contributed to this work. S. Cheon conceived and supervised the project. M. Kang constructed the models and analyzed the analytical results. Y. Prasad calculated the optical response of the system. N. D. Babu and R. Ghadimi compared the quantum weight and optical signatures. J. H. Kim presented experimental feasibility and potential implementation of this work. All authors participated in the writing of the manuscript.

* These authors contributed equally

† sangmocheon@hanyang.ac.kr

- [1] X.-L. Qi and S.-C. Zhang, Topological insulators and superconductors, *Reviews of modern physics* **83**, 1057 (2011).
- [2] L. Fu and E. Berg, Odd-parity Topological Superconductors: Theory and Application to $\text{Cu}_x\text{Bi}_2\text{Se}_3$, *Physical review letters* **105**, 097001 (2010).
- [3] S. D. Sarma, M. Freedman, and C. Nayak, Majorana zero modes and topological quantum computation, *npj Quantum Information* **1**, 1 (2015).
- [4] M. B. Hastings, C. Nayak, and Z. Wang, Metaplectic anyons, Majorana zero modes, and their computational power, *Physical Review B* **87**, 165421 (2013).
- [5] T. Sanno, M. G. Yamada, T. Mizushima, and S. Fujimoto, Engineering Yang-Lee anyons via Majorana bound states, *Physical Review B* **106**, 174517 (2022).
- [6] Y. You and F. von Oppen, Building fracton phases by Majorana manipulation, *Physical review research* **1**, 013011 (2019).
- [7] A. Nahum and B. Skinner, Entanglement and dynamics of diffusion-annihilation processes with Majorana defects, *Physical Review Research* **2**, 023288 (2020).
- [8] A. Y. Kitaev, Unpaired Majorana fermions in quantum wires, *Physics-усpekhi* **44**, 131 (2001).
- [9] Y. S. Hor, A. J. Williams, J. G. Checkelsky, P. Roushan, J. Seo, Q. Xu, H. W. Zandbergen, A. Yazdani, . f. N. Ong, and R. J. Cava, Superconductivity in $\text{Cu}_x\text{Bi}_2\text{Se}_3$ and its Implications for Pairing in the Undoped Topological Insulator, *Physical review letters* **104**, 057001 (2010).
- [10] S. Sasaki, M. Kriener, K. Segawa, K. Yada, Y. Tanaka, M. Sato, and Y. Ando, Topological superconductivity in $\text{Cu}_x\text{Bi}_2\text{Se}_3$, *Physical review letters* **107**, 217001 (2011).
- [11] L. Fu and C. L. Kane, Superconducting Proximity Effect and Majorana Fermions at the Surface of a Topological Insulator, *Physical review letters* **100**, 096407 (2008).
- [12] M. Z. Hasan and C. L. Kane, Colloquium: Topological insulators, *Reviews of modern physics* **82**, 3045 (2010).
- [13] T. D. Stanescu, J. D. Sau, R. M. Lutchyn, and S. Das Sarma, Proximity effect at the superconductor-topological insulator interface, *Physical Review B* **81**, 241310 (2010).
- [14] A. M. Black-Schaffer and A. V. Balatsky, Proximity-induced unconventional superconductivity in topological insulators, *Physical Review B* **87**, 220506 (2013).
- [15] C. Trang, N. Shimamura, K. Nakayama, S. Souma, K. Sugawara, I. Watanabe, K. Yamauchi, T. Oguchi, K. Segawa, T. Takahashi, et al., Conversion of a conventional superconductor into a topological superconductor by topological proximity effect, *Nature communications* **11**, 159 (2020).
- [16] K. Park, G. Csire, and B. Ujfalussy, Proximity effect in a superconductor-topological insulator heterostructure based on first principles, *Physical Review B* **102**, 134504 (2020).
- [17] S.-S. N. Devices, Signatures of majorana fermions in hybrid, *Cell* **81**, 967 (1995).
- [18] A. Das, Y. Ronen, Y. Most, Y. Oreg, M. Heiblum, and H. Shtrikman, Zero-bias peaks and splitting in an Al-InAs nanowire topological superconductor as a signature of Majorana fermions, *Nature Physics* **8**, 887 (2012).
- [19] M. Deng, S. Vaitiekėnas, E. B. Hansen, J. Danon, M. Leijnse, K. Flensberg, J. Nygård, P. Krogstrup, and C. M. Marcus, Majorana bound state in a coupled quantum-dot hybrid-nanowire system, *Science* **354**, 1557 (2016).

[20] M.-X. Wang, C. Liu, J.-P. Xu, F. Yang, L. Miao, M.-Y. Yao, C. Gao, C. Shen, X. Ma, X. Chen, *et al.*, The Coexistence of Superconductivity and Topological Order in the Bi_2Se_3 Thin Films, *Science* **336**, 52 (2012).

[21] P. Zareapour, A. Hayat, S. Y. F. Zhao, M. Kreshchuk, A. Jain, D. C. Kwok, N. Lee, S.-W. Cheong, Z. Xu, A. Yang, *et al.*, Proximity-induced high-temperature superconductivity in the topological insulators Bi_2Se_3 and Bi_2Te_3 , *Nature communications* **3**, 1056 (2012).

[22] J. Williams, A. Bestwick, P. Gallagher, S. S. Hong, Y. Cui, A. S. Bleich, J. Analytis, I. Fisher, and D. Goldhaber-Gordon, Unconventional Josephson Effect in Hybrid Superconductor-Topological Insulator Devices, *Physical review letters* **109**, 056803 (2012).

[23] M. Veldhorst, M. Snelder, M. Hoek, T. Gang, V. Guduru, X. Wang, U. Zeitler, W. G. van der Wiel, A. Golubov, H. Hilgenkamp, *et al.*, Josephson supercurrent through a topological insulator surface state, *Nature materials* **11**, 417 (2012).

[24] J.-P. Xu, M.-X. Wang, Z. L. Liu, J.-F. Ge, X. Yang, C. Liu, Z. A. Xu, D. Guan, C. L. Gao, D. Qian, *et al.*, Experimental Detection of a Majorana Mode in the core of a Magnetic Vortex Inside a Topological Insulator-Superconductor $\text{Bi}_2\text{Te}_3/\text{NbSe}_2$ Heterostructure, *Physical review letters* **114**, 017001 (2015).

[25] R. Valdés Aguilar, A. Stier, W. Liu, L. Bilbro, D. George, N. Bansal, L. Wu, J. Cerne, A. Markelz, S. Oh, *et al.*, Terahertz Response and Colossal Kerr Rotation from the Surface States of the Topological Insulator Bi_2Se_3 , *Physical review letters* **108**, 087403 (2012).

[26] P. Di Pietro, F. M. Vitucci, D. Nicoletti, L. Baldassarre, P. Calvani, R. Cava, Y. S. Hor, U. Schade, and S. Lupi, Optical conductivity of bismuth-based topological insulators, *Physical Review B* **86**, 045439 (2012).

[27] C. S. Tang, B. Xia, X. Zou, S. Chen, H.-W. Ou, L. Wang, A. Rusydi, J.-X. Zhu, and E. E. Chia, Terahertz conductivity of topological surface states in $\text{Bi}_{1.5}\text{Sb}_{0.5}\text{Te}_{1.8}\text{Se}_{1.2}$, *Scientific Reports* **3**, 3513 (2013).

[28] P. Törmä, S. Peotta, and B. A. Bernevig, Superconductivity, superfluidity and quantum geometry in twisted multilayer systems, *Nature Reviews Physics* **4**, 528 (2022).

[29] S. A. Chen and K. T. Law, Ginzburg-landau theory of flat-band superconductors with quantum metric, *Physical Review Letter* **132**, 026002 (2024).

[30] T. Liu, X.-B. Qiang, H.-Z. Lu, and X. C. Xie, Quantum geometry in condensed matter, *National Science Review* **12**, nwae334 (2024), <https://academic.oup.com/nsr/article-pdf/12/3/nwae334/59204701/nwae334.pdf>.

[31] B. Ghosh, Y. Onishi, S.-Y. Xu, H. Lin, L. Fu, and A. Bansil, Probing quantum geometry through optical conductivity and magnetic circular dichroism, *Science Advances* **10**, eado1761 (2024).

[32] Y. Onishi and L. Fu, Quantum weight: A fundamental property of quantum many-body systems, *Physical Review Research* **7**, 023158 (2025).

[33] N. Verma and R. Queiroz, Framework to measure quantum metric from step response, *Physical Review Letters* **134**, 106403 (2025).

[34] Y. Onishi and L. Fu, Fundamental bound on topological gap, *Physical Review X* **14**, 011052 (2024).

[35] L. Fu and C. L. Kane, Topological insulators with inversion symmetry, *Physical Review B—Condensed Matter and Materials Physics* **76**, 045302 (2007).

[36] J. R. Schrieffer and P. A. Wolff, Relation between the Anderson and Kondo Hamiltonians, *Physical Review* **149**, 491 (1966).

[37] W. Zimmermann, E. H. Brandt, M. Bauer, E. Seider, and L. Genzel, Optical conductivity of bcs superconductors with arbitrary purity, *Physica C* **183**, 99 (1991).

[38] K. I. Sim, Y. C. Jo, T. Ha, J. H. Kim, J. H. Kim, and H. Yamamori, Terahertz electrodynamics and superconducting energy gap of nbn, *Journal of the Korean Physical Society* **71**, 571 (2017).

[39] J. Provost and G. Vallee, Riemannian structure on manifolds of quantum states, *Communications in Mathematical Physics* **76**, 289 (1980).

[40] H. B. Callen and T. A. Welton, Irreversibility and generalized noise, *Physical Review* **83**, 34 (1951).

[41] I. Souza, T. Wilkens, and R. M. Martin, Polarization and localization in insulators: Generating function approach, *Physical Review B* **62**, 1666 (2000).

[42] H. Zhang, C.-X. Liu, X.-L. Qi, X. Dai, Z. Fang, and S.-C. Zhang, Topological insulators in Bi_2Se_3 , Bi_2Te_3 and Sb_2Te_3 with a single Dirac cone on the surface, *Nature physics* **5**, 438 (2009).

[43] C.-X. Liu, X.-L. Qi, H. Zhang, X. Dai, Z. Fang, and S.-C. Zhang, Model Hamiltonian for topological insulators, *Physical Review B* **82**, 045122 (2010).

[44] H. Bi and J. J. He, Vertical optical transitions of helical majorana edge modes in topological superconductors, *Physical Review B* **109**, 214513 (2024).

[45] J. E. Lee, J. Choi, T. S. Jung, J. H. Kim, Y. J. Choi, K. I. Sim, Y. Jo, and J. H. Kim, Gapless superconductivity in Nb thin films probed by terahertz spectroscopy, *Nature communications* **14**, 2737 (2023).

[46] F. Schindler, Dirac equation perspective on higher-order topological insulators, *Journal of Applied Physics* **128** (2020).

[47] R. Jackiw and C. Rebbi, Solitons with fermion number $\frac{1}{2}$, *Physical Review D* **13**, 3398 (1976).

[48] R. Jackiw and J. R. Schrieffer, Solitons with fermion number $\frac{1}{2}$ in condensed matter and relativistic field theories, *Nuclear Physics B* **190**, 253 (1981).